Operando Spectroscopic Insights into the Key Role of Phase Engineering in Cobalt Diselenide for Overall Water Electrolysis

Yonggui Zhao,* [a] Nanchen Dongfang,[a] Rolf Erni,[b] Marcella Iannuzzi,[a] and Greta R. Patzke*[a]

aDepartment of Chemistry, University of Zurich, Winterthurerstrasse 190, CH-8057 Zurich, Switzerland

E-mail: yonggui.zhao@chem.uzh.ch /greta.patzke@chem.uzh.ch

bElectron Electron Microscopy Center, Empa, Swiss Federal Laboratories for Materials Science and Technology, Überlandstrasse 129, CH-8600 Dübendorf, Switzerland

*Corresponding author

ABSTRACT: Identification of the true catalytically active species/sites holds the key to new catalyst design. In this study, combination of complementary *operando* surface/bulk sensitive spectroscopic techniques and density functional theory (DFT) calculations establish a clear picture of the structure-activity relations in marcasite- and pyrite-type $CoSe_2$ for overall water splitting. Our results reveal that under acidic conditions marcasite $CoSe_2$ undergoes slight surface corrosion, producing disordered $[CoSe_6]$ motifs with the active Se sites for catalyzing the hydrogen evolution reaction (HER). In contrast, during the alkaline HER, the marcasite $CoSe_2$ initially interacts with the electrolyte to reconstruct an O-rich covered surface, which subsequently undergoes potential-driven restructuring to generate the metallic cobalt species as the true active species. Such dynamic changes of the active species/sites along with variations in pH values were not observed in pyrite $CoSe_2$, either with or without heteroatom substitution, highlighting the significant importance of phase engineering in managing the HER kinetics. Further *operando* spectroelectrochemical monitoring demonstrates that the *in situ* generation of highly disordered Co^{4+} species is a common denominator of $CoSe_2$ catalysts for the oxygen evolution reaction (OER). This study directly evidences the dynamic influence of local coordination geometries of the catalytic active centers on the underlying catalytic reaction kinetics.

INTRODUCTION

The generation of green hydrogen as a renewable energy carrier via water electrolysis is pivotal in addressing the interconnected challenges posed by fossil fuels.[1–3] To date, two main techniques, namely alkaline water electrolysis (AWE) and proton exchange membrane water electrolysis (PEMWE), stand out as the most viable options for industrial-scale clean hydrogen production.[4,5,6] AWE typically offers higher material compatibility, enabling the use of earth-abundant transition metals to reduce capital expenses. Meanwhile, the unique character of AWE also contributes to a longer electrolyzer lifetime of up to 10 years.[3] However, the ongoing request for highly effective OER catalysts to improve the overall H_2 production efficiency remains a limiting factor for transition metal-based AWE systems. Compared to AWE, PEMWE provides the advantage of operating water electrolysis at high current densities (>2 A/cm^2), while its locally acidic media calls for high-yield catalysts, typically restricted to costly platinum group metals (PGMs). Against this backdrop, development of new catalysts based on earth-abundant transition metals, which display high catalytic activity under both alkaline and acidic conditions, presents an alternative option for advancing the commercialization of industrial-scale water electrolysis.

Over the past decade, numerous non-PGM-based catalysts have been explored, demonstrating remarkable catalytic activities for water electrolysis, i.e. alloys,[7] chalcogenides,[8,9,10] coordination polymers,[6,11–13] intermetallics,[14] oxides,[15,16,17] (oxy)hydroxides,[18,19] and pnictides,[20,21] et al. Among these catalysts, their high electrical conductivity and admirable catalytic kinetics render transition metal chalcogenides (TMCs) attractive candidates for overall water electrolysis. Unfortunately, TMCs suffer from unfavorable thermodynamic stability compared to conventional transition metal oxides.[3,5,22,23] Under harsh operational conditions, one would expect that the ongoing reaction proceeds along with the self-oxidation of TMCs, raising a great challenge for identifying the true catalytically active species/sites and for understanding the underlying catalytic reaction mechanisms. In such cases, advanced *in situ/operando* characterization techniques have emerged as powerful tools to address these fundamental challenges.[2,24,25] For instance, $CoSe_2$, as a representative TMC-based material, shows great promise for catalyzing both the HER and OER due to its unique structural properties and electronic configurations.[10,26–29] Previous studies have revealed that the OER $CoSe_2$ catalysts undergo significant phase transformations during the reaction process, in which *in situ*-generated CoOOH-related species serve as a prerequisite for triggering the OER.[10] However, the open question, "*Do the oxidized anionic components play a role in the OER?*" remains to be elucidated. In sharp contrast, $CoSe_2$ is generally investigated as a robust material to catalyze the HER,[22,26,30] and the dynamics of its catalytically active species and sites during the HER remain to be fully understood. Notably, two main crystal phases, namely the orthorhombic phase (o-$CoSe_2$) with a marcasite-type structure and the cubic phase (c-$CoSe_2$) with

a pyrite-type structure, commonly exist in $CoSe_2$.[26,31] Structurally, both phases feature similar $[CoSe_6]$ octahedral motifs connected via characteristic Se-Se pairs. It has been demonstrated that o-$CoSe_2$ exhibits better HER activities compared to c-$CoSe_2$ under acidic conditions,[26] whereas the opposite trend is observed in alkaline media.[32] This raises several fundamental questions to be answered, such as "*Where does the intrinsic HER activity of CoSe₂ catalysts originate?*", "*What are the true catalytically active species and sites in CoSe₂ catalysts during the HER?*", and "*How does phase transformation influence the intrinsic HER activities?*". In this sense, *operando* monitoring of $CoSe_2$ catalysts for the HER in different media is essential. Furthermore, the crucial role of phase engineering and oxidized anionic residues in the OER must also be clearly elucidated.

Herein, we implemented complementary *operando* time-resolved X-ray absorption spectroscopy (XAS) and Raman spectroscopy to establish a comprehensive understanding of the true catalytically active species and sites in $CoSe_2$ catalysts for overall water electrolysis. Three main materials, namely o-$CoSe_2$, c-$CoSe_2$, and c-$CoSe_2$ with partial sulphur substitution (denoted as c-S-$CoSe_2$), were synthesized and selected as model catalysts to *in situ* unravel the critical influence of phase engineering on the structural kinetics of $CoSe_2$ for water electrolysis in different media. For the first time, our *operando* results unravel distinct electrochemically driven restructuring behaviors in o-$CoSe_2$ for the HER under varying pH conditions. Specifically, under acidic conditions, o-$CoSe_2$ undergoes a pre-activation process with the removal of surface oxidized

oxyanions, after which the reconstructed o-$CoSe_2$ retains its structural integrity throughout the entire HER. In sharp contrast, for the alkaline HER, the pre-activation process promotes surface oxidation of anionic species and facilitates an exchange reaction between these oxidized species and the electrolytes. Subsequently, cathodic polarizations trigger an electrochemically driven restructuring, generating metallic Co species that act as the true catalytically active species. Notably, such pH-dependent restructuring phenomena are absent in c-$CoSe_2$ and c-S-$CoSe_2$ during the HER, highlighting the significance of phase engineering in regulating the reaction kinetics. As for the OER, our results corroborate that *in situ*-generated defective CoO_2 species contribute to the intrinsic OER activities of all $CoSe_2$ catalysts. Additionally, surface oxidized anionic components undergo complete dissolution into the electrolyte and do not contribute to the OER. This conclusion is further supported by our OER characterizations performed on reference o-$CoSe_2$ catalysts with partial phosphorus incorporation (denoted as o-P-$CoSe_2$) under identical reaction conditions. Furthermore, combined *operando* monitoring and DFT calculations allow us to establish a detailed intrinsic structure-activity relationship in $CoSe_2$ catalysts for water electrolysis under operational conditions.

RESULTS AND DISCUSSION

Materials synthesis and characterization

To synthesize $CoSe_2$ catalysts (i.e. o-$CoSe_2$, c/o-$CoSe_2$, c-$CoSe_2$, and c-S-$CoSe_2$), hierarchical ZIF-67 precursors were first fabricated using a room-temperature anion-exchange
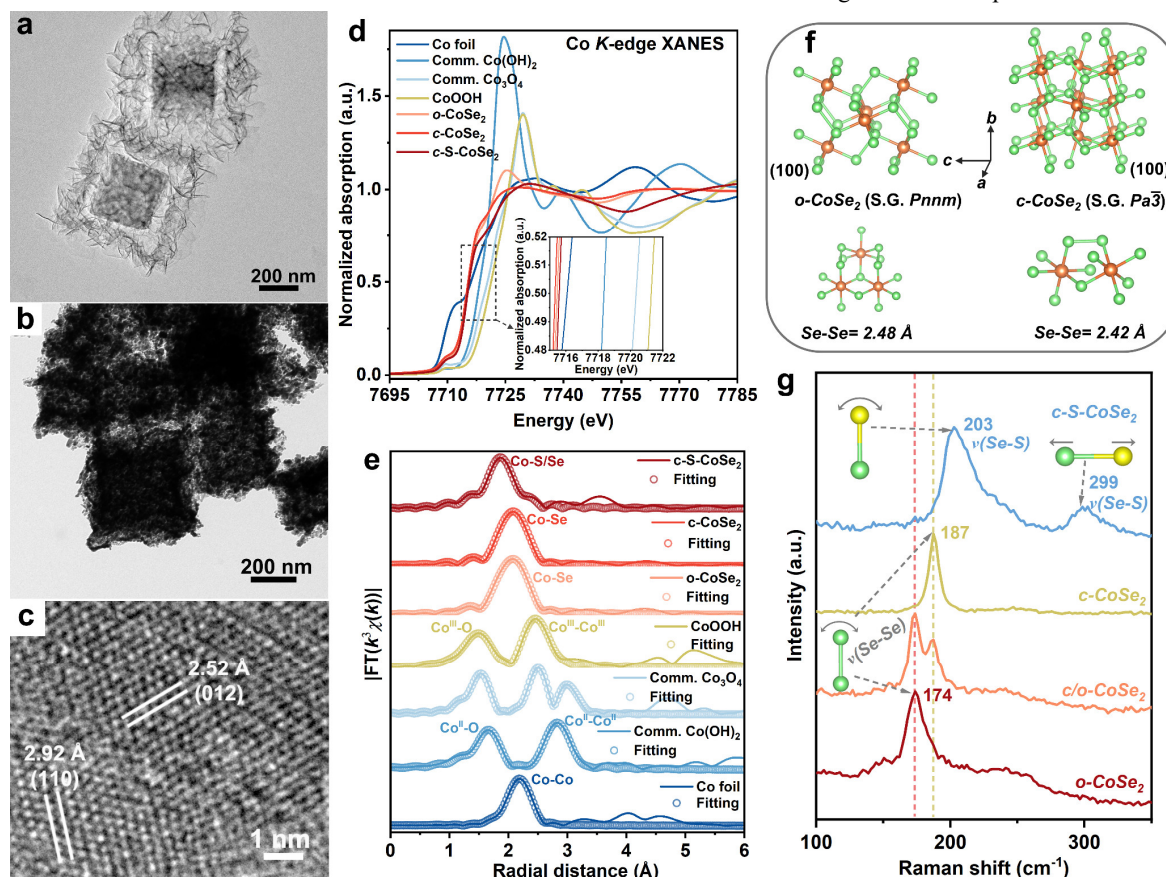

Figure 1. Morphological and structural characterizations of the investigated catalysts. TEM images of hierarchical ZIF-67 (a) and o-$CoSe_2$ (b). (c) HR-TEM image of o-$CoSe_2$. (d, e) Co *K*-edge XANES spectra and fitting of FT-EXAFS spectra of as-investigated samples vs. references. (f) Structural models of o-$CoSe_2$ and c-$CoSe_2$. (g) Raman spectra of $CoSe_2$-related materials. (**Note**: green spheres = Se; orange spheres = Co; yellow spheres = S)

2

approach and subsequently employed as the template (**see Experimental Methods, Figure S1**). As illustrated by field-emission scanning electron microscopy (FESEM) and transmission electron microscopy (TEM) (**Figure 1a and Figures S2-S4**), yolk-shell nano cubic architectures are evident in the as-prepared ZIF-67 precursors. Followed by a conventional selenylation/sulphuration process, the o-$CoSe_2$, c/o-$CoSe_2$, c-$CoSe_2$, and c-S-$CoSe_2$ nanoarchitectures were successfully fabricated. Then, a wide range of characterization techniques were employed to explore the morphological and structural properties of the as-prepared products. From the results (**Figure 1b and Figures S5-S11**), the pristine nano cubic architectures of ZIF-67 precursors were well preserved in the as-synthesized $CoSe_2$ samples. Analysis of high-resolution TEM (HR-TEM) characterizations (**Figure 1c and Figure S7**) unravels interplanar spacings of 2.42, 2.52, and 2.92 Å, corresponding to the main exposed (020), (012), and (110) planes, respectively, reflecting the orthorhombic structures of the as-synthesized o-$CoSe_2$ (PDF no. 09-0234, **Figure S5a**). Note that the synthetic parameters (i.e. reaction temperature and heating rate) play a key role in the formation of $CoSe_2$ with different crystal phases, i.e., o-$CoSe_2$ (350 °C at 2 °C/min), c/o-$CoSe_2$ (400 °C at 2 °C/min), and c-$CoSe_2$ (400 °C at 5 °C/min), as confirmed by the powder X-ray diffraction (PXRD) patterns (**Figure S5a-c**). Partial sulphur incorporation into $CoSe_2$ resulted in the formation of c-S-$CoSe_2$, and the observed characteristic diffraction peaks in its PXRD pattern (**Figure S5d**) show a shift towards a higher 2 θ position compared to the standard c-$CoSe_2$ (PDF no. 09-0234). This infers that the introduction of S ions results in a decrease in the lattice parameters of $CoSe_2$ because of its smaller atomic radius than the Se ions. Furthermore, a reference o-P-$CoSe_2$ sample was synthesized to gain in-depth insights into the intrinsic catalytic mechanisms (**Figure S12**). The PXRD results (**Figure S12a**) indicate that the as-prepared o-P-$CoSe_2$ matches well with the o-$CoSe_2$ phase (PDF no. 53-0449).

Electronic structure and coordination environment analysis

The local electronic structures and coordination environments of $CoSe_2$ materials were analyzed through *ex situ* XAS characterizations (**Figure 2d,e and Figure S13**). Corresponding *ex situ* Co *K*-edge X-ray absorption near-edge structure (XANES) spectra shown in **Figure 2d** unravel a similar line shape in the rising absorption edge of $CoSe_2$ materials, indicating comparable local coordination geometries of Co centers coordinated by Se atoms. A close examination of the Co *K*-edge XANES spectra (~7725 eV) highlights prominent white line features of o-$CoSe_2$ compared to c-$CoSe_2$ and c-S-$CoSe_2$. This infers that surface oxidation is more accessible for the as-prepared o-$CoSe_2$ than for the other phase samples.[8,20] Co *K*-edge Fourier-transform extended X-ray absorption fine structure (FT-EXAFS) characterizations were further conducted to identify the local coordination environments of Co centers of the investigated samples. The results show (**Figure 2e**) that all $CoSe_2$ samples feature only one intense peak within the interval of R+ΔR = 1 to 3 Å, corresponding to the backscattering of Co-Se/S pairs. Notably, the observed backscattering signal of c-S-$CoSe_2$ exhibits a distinct negative position shift compared to c-$CoSe_2$ and c-S-$CoSe_2$, due to the shorter interatomic distance of the Co-S bond relative to the Co-Se bond, as supported by the fitting results of Co *K*-edge EXAFS spectra (**Table S1**). Precise identification of the local coordination environments of Co centers in o-$CoSe_2$

and c-$CoSe_2$ is challenging because both feature similar [$CoSe_6$] octahedra motifs (**Figure 1f**). However, the interatomic distance of the characteristic Se-Se pairs in o-$CoSe_2$ is slightly larger than the one in c-$CoSe_2$. Such a difference can be monitored by the Raman spectra due to its sensitivity to the librational vibrations of characteristic Se-Se pairs (**Figure 1g and Figure S14**).[33] As expected, o-$CoSe_2$ features its characteristic Se-Se librational vibration at ca. 174 cm⁻¹, which undergoes a positive Raman shift to ca. 187 cm⁻¹ when the c-$CoSe_2$ phase is present.[26,30,32] Partial S incorporation into c-$CoSe_2$ leads to the construction of S-Se pairs with a further decrease in the interatomic distance, and the characteristic Raman signals shift to a higher wavenumber at ca. 203 cm⁻¹ accordingly. It is also noteworthy that partial S incorporation produces newly formed Raman signatures at ca. 299 and 490 cm⁻¹, which can be assigned to the stretching vibrations of S-Se and Co-S/Se pairs, respectively.[33,34]

Electrochemical performance characterizations

Engineering of crystal phase regulation or introduction of heteroatom emerges as an effective strategy to facilitate the underlying catalytic reaction kinetics, thereby optimizing the electrocatalytic performances of many reported catalysts.[10,13,26,28,29] To evaluate the electrochemical water splitting performance, the as-prepared $CoSe_2$ catalysts were assembled as both cathodic and anodic electrodes for the HER and OER in different media. Note that the recorded linear sweep voltammetry curves were normalized by the electrochemical active surface area (ECSA) with a 90% iR drop correction to ensure a more accurate assessment of the intrinsic catalytic activities (**Figures S15-S17**).[35]

HER characterization at pH 0 and 14. The electrochemical HER performance of the as-prepared $CoSe_2$ catalysts was evaluated at both pH 0 and 14. Under acidic conditions (**Figure 2a,d and Figure S17a,d,g**), the as-prepared c-S-$CoSe_2$ displays the best HER performance with an overpotential of -94 mV (-88 mV) at the current density of -0.5 mA/cm$_{ECSA}^2$ (-10 mA/cm$_{geo.}^2$), a Tafel slope value of 64.02 mV/dec, and a charge transfer resistance of 8.7 Ω, which outperformed those of o-$CoSe_2$ (-164 mV/-149 mV, 78.19 mV/dec, and 72.4 Ω), c/o-$CoSe_2$ (-182 mV/-159 mV, 78.19 mV/dec, and 84.4 Ω), and c-$CoSe_2$ (-200 mV/-217 mV, 78.19 mV/dec, and 355.1 Ω). Moreover, the electrochemical stability results corroborate that the investigated catalysts maintain their initial HER activities after 300 h without any obvious changes (**Figure 2g**). In sharp contrast, under alkaline conditions (**Figure 2b,e,h and Figure S17b,e,h**), the best HER performance can be still achieved in c-S-$CoSe_2$, while the other $CoSe_2$ catalysts exhibit a disparate activity order compared to acidic conditions: c-$CoSe_2$ > c/o-$CoSe_2$ > o-$CoSe_2$. These results altogether unravel that crystal phase engineering or heteroatom substitution plays a pivotal role in optimizing the HER kinetics of $CoSe_2$ catalysts in different media, which calls for *operando* unraveling the true chemical nature of active species and sites during the reaction processes.

OER characterization at pH 14. The OER process emerges as the bottleneck for effective water electrolysis. Therefore, we further employed the as-prepared $CoSe_2$ catalysts as anodic materials for the OER at pH 14. As demonstrated in **Figure 2c,f and Figure S17c,f**, to achieve a current density of 0.02
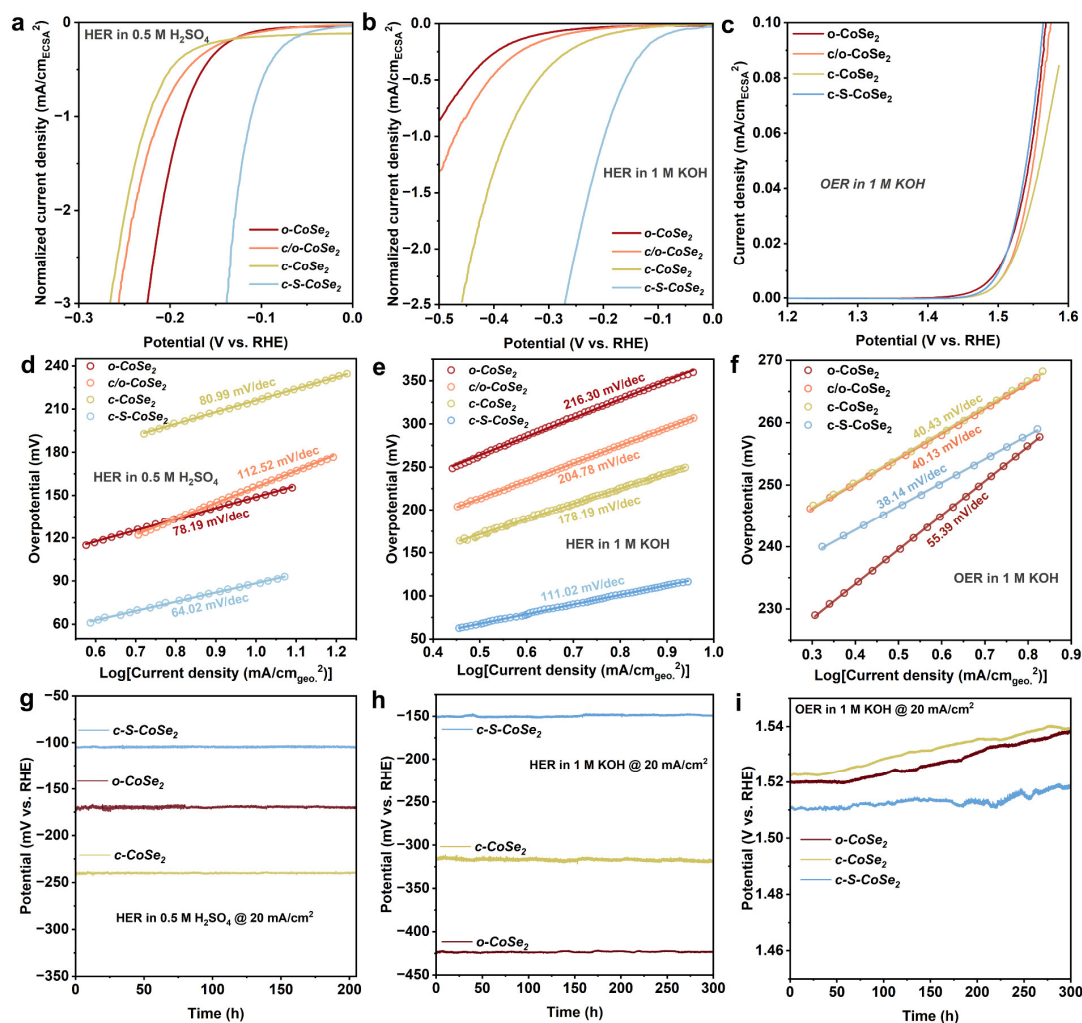
3

Figure 2. Electrochemical characterizations of the as-prepared catalysts for water electrolysis in different media. Normalized LSV curves of the as-prepared catalysts in 0.5 M H_2SO_4 for the HER (a), in 1 M KOH for the HER (b), and in 1 M KOH for the OER (c). (b-f) Tafel plots of the as-prepared catalysts for the HER and OER in different media. (g-i) Long-time stability measurements of the as-prepared catalysts loaded on carbon paper.

mA/cm_{ECSA}^2 or 10 $mA/cm_{geo.}^2$, a minimum overpotential of 286 mV or 266 mV is required for c-S-CoSe$_2$, close to those of o-CoSe$_2$ (287 mV or 269 mV), c/o-CoSe$_2$ (296 mV or 275 mV), and c-CoSe$_2$ (300 mV or 276 mV). The electrochemical durability results (**Figure 2i**) indicate that all the investigated CoSe$_2$ catalysts retain their initial OER performance for 300 h with a slight potential increase. Besides, rotating-ring disk electrode (RRDE) experiments (**Figure S18a**) demonstrate a nearly 100% Faradaic efficiency for c-S-CoSe$_2$, indicating that the OER predominantly occurs on the electrode surface. From the above results (**Figure 2c,f,i and Figure S17c,f,i**), one can also notice that there were no significant OER performance differences in the as-synthesized CoSe$_2$ catalysts. This is because under the OER conditions CoSe$_2$ catalysts are expected to undergo restructuring into their corresponding oxides/hydroxides, which serve as a prerequisite to initiate the OER.[5,23,36] However, the critical role of oxidized oxyanion components (i.e. SeO$_x^-$ and SO$_x^-$) in the OER of the investigated catalysts remains to be fully elucidated. This requires *operando* time-resolved monitoring of the investigated catalysts under operational reaction conditions, which will be discussed in detail in the following section on *operando* characterizations.

Dynamics of active species and sites

To gain in-depth insights into the origins of the intrinsic catalytic activities and the underlying structural kinetics of CoSe$_2$ catalysts in different media, we first performed *ex situ* XPS characterizations for the catalysts before and after water electrolysis [**Note**: In this study, "post-catalytic characterization" refers to samples subjected to electrochemical stability tests, as shown in the durability measurements in **Figure 2 g-i**]. From the results (**discussion details in Figures S19-S21**), except for o-CoSe$_2$, the investigated CoSe$_2$ catalysts remain stable for the HER at both pH 0 and 14, while after the OER all catalysts undergo complete surface restructuring into oxide/hydroxide species without any prominent oxidized anionic components adsorbed on the surface. To precisely identify the true catalytically active species and to establish an identical structure-activity relationship during the water electrolysis process, *operando* time-resolved XAS and Raman spectra characterizations were further carried out.

HER monitoring and kinetics at pH 0. We first performed *operando* Co *K*-edge XAS characterizations for o-CoSe$_2$ to monitor the chemical nature of Co centers during the acidic HER (**Figure 3a,b and Figures S22 and S23**). From the *operando* Co *K*-edge XANES monitoring (**Figure 3a**), it is found that the spectral features at ca. 7725 eV, associated with

4

the dipolar transitions from Co 1*s* to 4*p* hybridized orbitals,[8,20,24] undergo a remarkable profile change along with the cathodic polarizations. In detail (**Figure 3a**), the white line signatures feature profile changes towards lower peak intensities prior to the cathodic polarization, and then they remain almost identical throughout the *operando* monitoring experiments. This points out that during the acidic HER o-CoSe$_2$ experiences a surface etching process, resulting in the removal of the surface oxidized species, and the reconstructed o-CoSe$_2$ subsequently performs the role of the acidic HER. The Co valence state was analyzed through a linear exploration of the rising absorption edge position of the Co *K*-edge XANES spectra. As illustrated in the inset plot of **Figure 3a**, a sharp decrease in the Co valence state can be observed upon immersion of the catalysts into the electrolyte; with the cathodic polarization, the Co valence state undergoes a slight further decrease before stabilizing during the HER. Note that the observed oscillation features of the *operando* Co *K*-edge EXAFS spectra (**Figure S22**) for o-CoSe$_2$ remain nearly unchanged throughout the acidic HER, demonstrating an identical local coordination geometry of Co centers. Analysis of the fitting of *operando* Co K-edge FT-EXAFS spectra (**Figure 3b, Figure S23, and Table S2**) clearly reveals the removal of surface oxidized species when the catalysts are immersed into the electrolyte, evidenced by a sharp decrease in the coordination numbers of the first Co-O shells (CN$_{Co-O}$). In contrast, the CN$_{Co-Se}$ value barely changes during the acidic HER.

Operando Raman spectra characterizations were conducted to shed light on the surface kinetics of o-CoSe$_2$ during the acidic HER. As demonstrated in **Figure 3c**, the characteristic Se-Se librational vibrations were preserved well during the acidic HER. Besides, five newly formed Raman signatures appeared

at 428, 592, 896, 983, and 1052 cm^{-1} can be also observed during the cathodic polarizations, originating from the adsorption of H$_2$SO$_4$ electrolytes on the electrode surface.[37] Identification of the nature of adsorbed SeO$_x^-$ species on o-CoSe$_2$ under acidic conditions is challenging, as their vibration fingerprints overlapped with those of v(HSO$_4^-$) (**Figure 2c**). To gain in-depth insights into the surface kinetics of o-CoSe$_2$ during the acidic HER, inductively coupled plasma mass spectrometry (ICP-MS) analysis was performed for the electrolyte before and after the reaction. The results (**Table S3**) showed a slight increase in the concentrations of Co and Se elements in the electrolyte after the HER, reflecting the dissolution of surface oxidized species into the electrolyte. Based on the above, one can conclude that during the acidic HER the investigated o-CoSe$_2$ electrode experiences surface corrosion with the dissolution of surface oxidized oxyanion into the electrolytes, and thereafter the resulting electrode retains its structural integrity well for catalyzing the acidic HER (**Figure S24**).

HER monitoring and kinetics at pH 14. The origins of the intrinsic HER activities and the underlying reaction kinetics of o-CoSe under alkaline conditions were also investigated via *operando* XAS and Raman spectra characterizations (**Figure 4d-f and Figures S25-S28**). **Figure 4d** presents the *operando* time-resolved Co *K*-edge XANES spectra of o-CoSe$_2$ during the HER at pH 14. One can notice that the characteristic spectral features of Co 1*s* to 4*p* hybridized orbitals display a disparate profile change during the alkaline HER compared to the observations during the acidic HER. In detail, from immersing the catalysts into the electrolyte to the alkaline HER, their peak intensities first undergo a significant enhancement along with an increased Co valence state (**Figure 4a and Figure S25**). Then, these key features decreased drastically as the applied
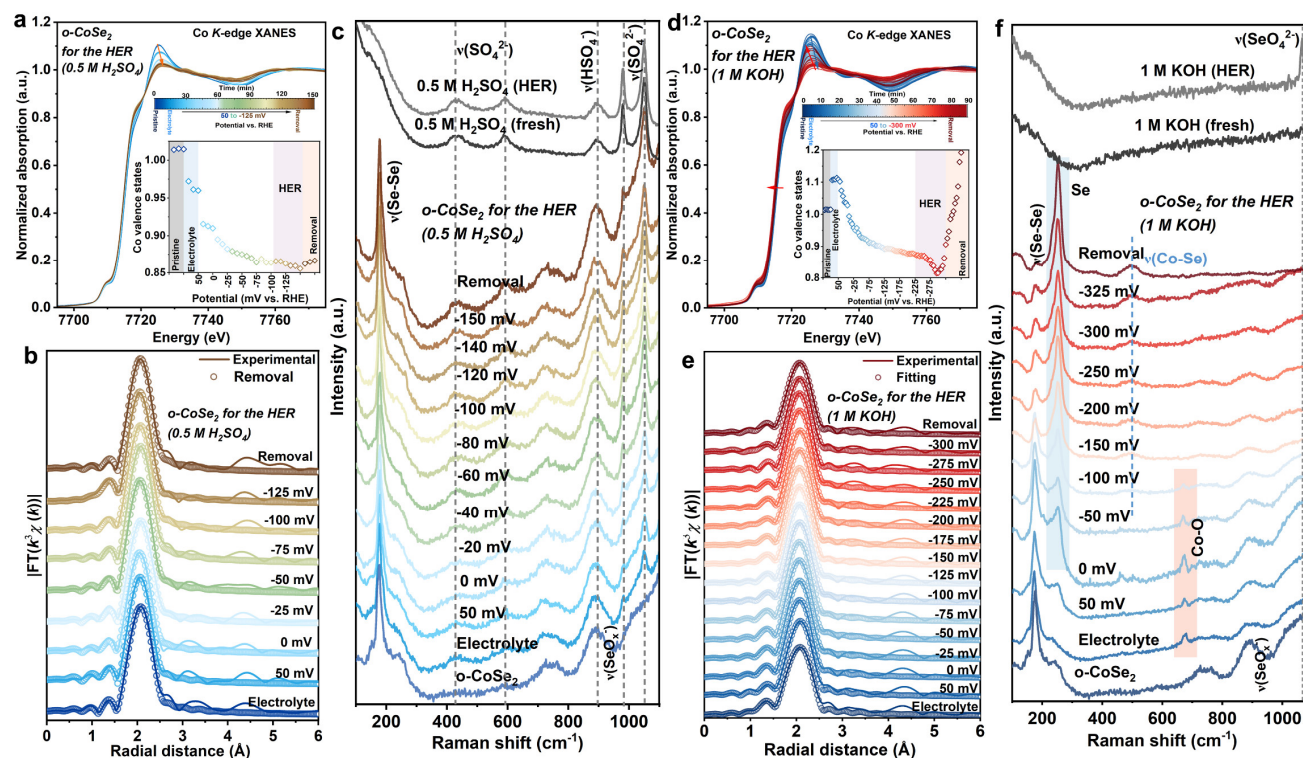

Figure 3. *Operando* XAS and Raman spectra characterizations of o-CoSe$_2$ for the HER. (a and d) *Operando* Co K-edge XANES spectra at pH 0 and 14. (b and e) Fitting of *operando* Co K-edge FT-EXAFS spectra at pH 0 and 14. (c and f) *Operando* Raman spectra at pH 0 and 14.

5

potential decreased from 50 to -100 mV vs. RHE, meanwhile, the Co valence states decreased from +1.11 to +0.90. For the applied potentials below -100 mV, the spectral features of Co 1*s* to 4*p* hybridized orbitals remain almost identical, but they revert to higher signal intensities after removing the applied potentials. In comparison, the Co valence states exhibit only a slight decrease from +0.90 to +0.87 for the applied potentials in the range -100 to -250 mV vs. RHE; a further decrease of the applied potentials to -300 mV vs. RHE leads to a distinct decrease in the Co valence states to +0.81. Notably, after the removal of the applied potentials, a significant increase in the Co valence states with a maximum value of +1.19 is observed. All these results suggest that o-CoSe$_2$ undergoes dynamic changes in the local coordination geometries of the catalytically active centers during the alkaline HER, in which the *in situ* generated low-valent Co species play a critical role in managing the underlying HER kinetics.

The dynamics of the local Co coordination environments in o-CoSe$_2$ during the HER at pH 14 were analyzed using *operando* time-resolved Co *K*-edge EXAFS and FT-EXAFS spectra (**Figure 4e and discussion and details in Figure S26**) as well. Analysis of the *operando* Co *K*-edge EXAFS spectra reveals that the Co centers in o-CoSe$_2$ undergo kinetic coordination geometric changes into metallic Co species during the HER. To precisely identify the local coordination environments of active Co centers in o-CoSe$_2$ during the alkaline HER, fitting of the *operando* Co *K*-edge FT-EXAFS spectra was performed. From the results (**Figure 4b, Figure S27, and Table S4**), it is found that the CN$_{Co-Se}$ value exhibits barely changes during the alkaline HER. In sharp contrast, the CN$_{Co-O}$ value shows a slightly increasing tendency upon immersion of the catalysts into the electrolyte, but thereafter it undergoes a continuous decreasing tendency, ultimately approaching zero under the cathodic polarizations. After the removal of the applied potentials, a significant increase in the CN$_{Co-O}$ value can be observed. These observations are also accordant with the above *operando* analysis on the Co valence states. On this basis, we propose that the investigated o-CoSe$_2$ catalysts undergo the following structural rearrangement and the reaction kinetics during the alkaline HER (**Figure S28**): (*i*) o-CoSe$_2$ experience surface oxidation along with a surface interaction with the electrolytes during the electrochemical pre-activation process, as supported by the increased Co valence states and CN$_{Co-O}$ values; (*ii*) investigations of the *operando* time-resolved Co *K*-edge XAS data suggest that the HER proceeds along with an electrochemically driven structural rearrangement from the reconstructed oxidized species absorbed on the surface into the low-valent metallic Co species, which act as the true catalytically active species; (iii) after the removal of the applied potentials, these active metallic Co species can further interact with the electrolytes and revert into oxide-related species as the HER resting species.

Such a surface interaction with the oxidized species further converts into active metallic Co species can be also evident from the *operando* Raman spectra analyses. As demonstrated in **Figure 4f**, with the cathodic polarizations, the characteristic Se-Se librational and SeO$_x^-$ signatures feature distinct profile changes towards weakened signal intensities. At the same time, a newly formed Raman signature at ca. 680 cm^{-1}, associating with the Co-O vibrations,[16,38,39] was first observed when the applied potentials were below 100 mV vs. RHE. A further decrease of the applied potentials results in the disappearance

of the aforementioned Co-O vibrations but generates newly formed Co-Se signatures. This points out that the initial reconstructed surface oxidized species on o-CoSe$_2$ undergoes a further restructuring into active Co species during the HER. It is also noteworthy that during the alkaline HER o-CoSe$_2$ features another significant Raman signature at ca. 252 cm^{-1}, which exhibits profile changes toward a higher signal intensity as the applied potential decreases. Previous studies indicated that the aforementioned vibrations feature a similar Raman fingerprint as amorphous Se species.[34] Besides, after the removal of the applied potentials, a distinct $v(SeO_4^{2-})$ Raman signal can be detected from the electrolytes. This observation is also consistent with the ICP-MS analysis (**Table S3**), in which a significant content of Se ions can be observed in the electrolyte after the HER. With the above *operando* XAS and Raman results, one can conclude that o-CoSe$_2$ undergoes a surface selenium-oxygen exchange reaction preceding the alkaline HER, and these *in-situ* generated oxidized species can further convert into catalytically active metallic Co species, accompanied by the leaching of oxyanion components into the electrolyte.

OER monitoring and kinetics at pH 14. Other than for the *operando* spectroscopic monitoring of the HER, we have also implemented *operando* time-resolved XAS and Raman characterizations to unveil the dynamics of active species and sites of o-CoSe$_2$ for the OER at pH 14 (**Figure 4 and Figures S29 and S30**). Analysis of the *operando* time-resolved Co *K*-edge XANES spectra (**Figure 4a**) shows that the white line signatures of the dipolar transitions from Co 1*s* to 4*p* hybridized orbitals display profile changes toward higher energy positions and enhanced signal intensities, inferring the oxidations of Co centers and the formation of Co-based oxides/hydroxides. An in-depth analysis of the *operando* time-resolved Co *K*-edge XAS data reveals that the Co valence state reaches its maximum value of ca. +2.70 at 1.5 V vs. RHE, while a slight decrease can be observed after the removal of the applied potential. This
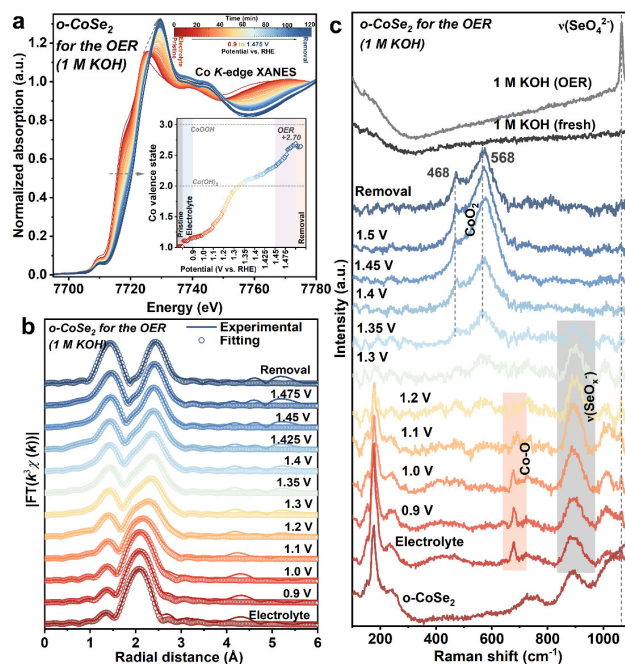

Figure 4. *Operando* **XAS and Raman spectra characterizations of o-CoSe$_2$ for the OER at pH 14.** (a) *Operando* Co *K*-edge XANES spectra. (b) Fitting of *operando* Co *K*-edge FT-EXAFS spectra. (c) *Operando* Raman spectra.

6

corroborates that the OER relies on the *in situ* generated catalytically active high-valent Co species, in agreement with many previous studies.[8,40,41] The local coordination environments of Co centers in o-CoSe$_2$ for the OER were investigated through *operando* time-resolved Co *K*-edge EXAFS and FT-EXAFS spectra monitoring(**Figure 4b**, **Figures S29 and S30, and Table S5**). Our *operando* time-resolved monitoring reveals that o-CoSe$_2$ undergoes potential-driven restructuring into defective CoO$_2$ species, which is a prerequisite to initiating the OER at pH 14. The crucial formation of the high-valent CoO$_2$ species derived from o-CoSe$_2$ during the OER can be also evident from *operando* Raman spectra characterizations (**Figure 4c**). As expected, during the alkaline OER, the characteristic Se-Se librational vibration signals feature drastic profile changes and are barely detected when the applied potentials are higher than 1.3 V vs. RHE. In sharp contrast, with the anodic polarizations, two newly formed vibration features at ca. 468 and 568 cm^{-1}, which are associated with CoO$_2$ species,[8,19,38,40,42,43] were first observed at 1.3 V vs. RHE, and then they exhibit profile changes towards higher signal intensities as the potentials increased. This is a piece of evidence to support that the *in situ*-generated high-valent CoO$_2$ species is the key to the O$_2$ release in o-CoSe$_2$. It is also noteworthy that the *operando* Raman spectra of o-CoSe$_2$ only feature ν(SeO$_x^-$) signals below 1.3 V vs. RHE. Such vibration signals are barely detected in the OER region (**Figure 4f**). Moreover, after the removal of the potential,

a remarkable ν(SeO$_4^{2-}$) signal in the post-catalytic electrolytes can be observed, suggesting that the surface oxidized anionic components in o-CoSe$_2$ undergo complete leaching into the electrolytes (**Table S3**), which is not decisive to the OER.

Role of phase engineering in the HER and OER

Combination of *operando* XAS and Raman spectra analysis unambiguously indicates that o-CoSe$_2$ undergoes a divergent electrochemically driven restructuring into corresponding catalytically active species during the water electrolysis in different media. To shed more light on the origins of the restructuring of CoSe$_2$ catalysts at different pH values, *operando* time-resolved XAS and Raman spectra characterizations for c-CoSe$_2$ and c-S-CoSe$_2$ were carried out as well (**Figures S31-S37**). For the HER at both pH 0 and pH 14, our results (**Figures S31, S32a,b, S33, S34, and S37a,b, and Tables S6-S8**) demonstrate that either c-CoSe$_2$ or c-S-CoSe$_2$ maintains their structural integrity well throughout the entire *operando* monitoring. Concerning the OER, our *operando* analyses (**Figures S31, S32c, S35, S36, and S37c, and Table S9**) unravel both c-CoSe$_2$ and c-S-CoSe$_2$ undergo a significant structural transformation into high-valent CoO$_2$ species to trigger the OER as to o-CoSe$_2$. Moreover, our *operando* results (**Figures S32c and S37c and Table S3**) also unveil that the surface oxidized oxyanions (i.e. SeO$_4^{2-}$ or SO$_4^{2-}$) in c-CoSe$_2$ and c-S-CoSe$_2$ are completely leached into the electrolyte during the
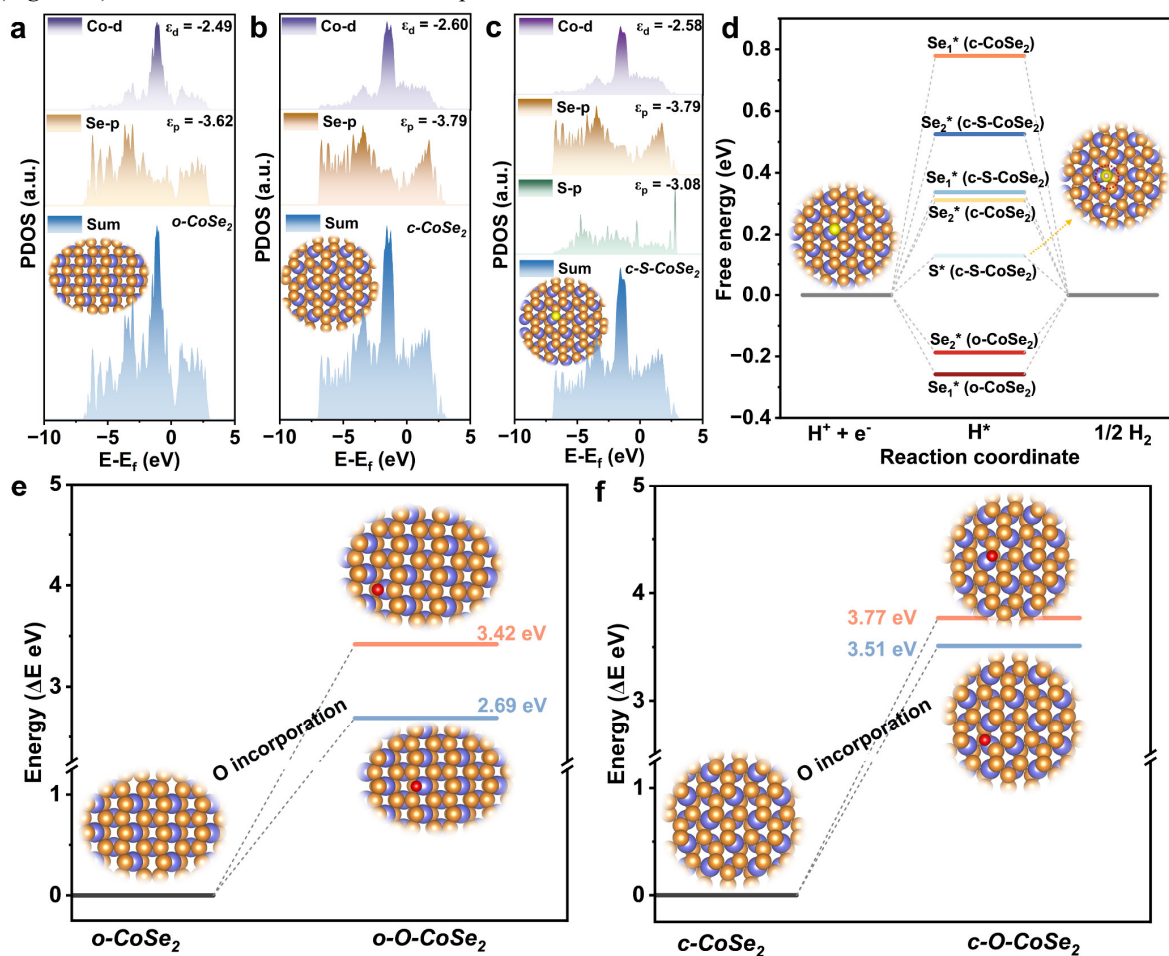

Figure 5. Calculated PDOS of o-CoSe$_2$ (a), c-CoSe$_2$ (b), and c-S-CoSe$_2$ (c). (d) Calculated free energy diagrams of H* intermediates adsorbed on three catalysts. Comparison of the calculated energy of o-CoSe$_2$ (e) and c-CoSe$_2$ (f) with and without O incorporation.

7

OER. However, the open question of whether trace amounts of the oxidized anionic residual play a role in the OER still needs to be elucidated. This open question can be well addressed by conducting the OER characterizations of partially P-incorporated o-CoSe$_2$ (o-P-CoSe$_2$) (**Figures S38 and S39**). This is because heteroatom doping has been demonstrated as an effective strategy to tune the OER kinetics of the catalysts.[10,13,43] As shown in **Figure S36**, no significant difference in the OER activity is observed between o-CoSe$_2$ and o-P-CoSe$_2$. Additionally, the post-catalytic Raman spectra clearly corroborate that the as-investigated o-P-CoSe$_2$ completely converts into CoOOH-like species without any oxidized anionic residual absorbed on the surface. This strongly supports that the surface oxidized oxyanions in CoSe$_2$ catalysts are not the key to initiating the OER. On the other hand, *operando* XAS results (**Tables S5, S6, and S9**) unambiguously unravel that the *in situ* restructured catalytically OER active species (i.e. CoO$_2$) derived from the as-investigated CoSe$_2$ catalysts feature significant structural disorder. As reported, engineering defective catalysts generally offer abundant active sites, thereby regulating the desorption/adsorption of key OER intermediates.[11,13,15,23,40,44] As a result of the tuned OER kinetics, employment of transition metal non-oxide catalysts enables a better OER performance compared to conventionally synthesized oxides.[8,20,23]

The intrinsic reaction mechanisms based on DFT simulations

To directly evidence the origins of the intrinsic catalytic activity and to precisely establish a full picture of the underlying reaction mechanisms, DFT simulations were conducted with the investigated CoSe$_2$ catalysts. **Figure 5a-c** represents the calculated projected density of states (PDOS) of the three catalysts. From the results, the Co d and Se/S p orbital states distributions spread over the Fermi level, reflecting the intrinsic metallic character of the CoSe$_2$ materials. According to previous studies, the d-p band center proximity (denoted as $\Delta\varepsilon_{d-p}$) is regarded as a key descriptor for elucidating the underlying HER kinetics.[45] Specifically, a smaller $\Delta\varepsilon_{d-p}$ enables facilitated electron mobility and optimization of the adsorption/desorption of H* intermediates on the active sites, thereby, offering a better HER activity. As shown in **Figure 5a,b**, o-CoSe$_2$ gives a $\Delta\varepsilon_{d-p}$ value of 1.13, which is noticeably smaller than that of c-CoSe$_2$ (1.19), pointing out a facilitated HER kinetics involved in o-CoSe$_2$ compared to c-CoSe$_2$. Partial S incorporation into CoSe$_2$ further reduces the $\Delta\varepsilon_{d-p}$ value to 0.50, ascribed to the newly induced Co d-S p orbital hybridization (**Figure 5c**). As a result of the optimized HER kinetics, the as-investigated c-S-CoSe$_2$ delivers the best HER performance compared to those of o-CoSe$_2$ and c-CoSe$_2$ (**Figure 2a**). This is further corroborated by the calculated adsorption free energy of H* intermediates (ΔG_{H*}) on the investigated three catalysts (**Figure 5d and Figures S40-S43**). Notably, KSCN poisoning experiments clearly reveal that the acidic HER activity is independent of the KSCN additive, indicating that the adsorption/desorption of H* intermediates primarily occurs at the Se/S sites (**Figure S40**). Based on this, our results (**Figure 5d**) show that the best-performing HER c-S-CoSe$_2$ catalyst features a minimum ΔG_{H*} value of 0.13 eV, which is smaller than those of o-CoSe$_2$ (0.19 eV) and c-CoSe$_2$ (0.31 eV). Furthermore, we calculated the formation energy required for partial oxygen incorporation into the investigated catalysts to gain in-depth insights into the HER kinetics under alkaline conditions. The results (**Figure 5e,f**)

indicate that for o-CoSe$_2$ a minimum energy barrier of 2.69 eV needs to be overcome for surface oxygen incorporation, which is lower than that of c-CoSe$_2$ (3.51 eV). This suggests that c-CoSe$_2$ is more thermodynamically stable than o-CoSe$_2$ towards the alkaline HER, in agreement with our above *operando* monitoring (**Figure 3 and Figures S29-S37**). As discussed extensively in the previous *operando* monitoring section, the *in situ* generated low-valent Co species are identified as decisive factors to trigger the alkaline HER, therefore, we further calculated the ΔG_{H*} value for the H* intermediates adsorbed on the Co sites in o-CoSe$_2$ with rich Co exposure. The results (**Figure S44**) reveal that a minimum ΔG_{H*} value of 0.27 eV is determined in the o-CoSe$_2$ with rich Co exposure, which is significantly higher than that of the Se sites (0.13 eV), indicating a sluggish HER kinetics proceeds at the Co sites at pH 14. In other words, the above analysis also offers a clear explanation for why o-CoSe$_2$ catalysts feature poor electrochemical HER performance at pH 14 compared to pH 0 (**Figure 2**).

Conclusion

In summary, with the help of *operando* time-resolved XAS and Raman spectra characterizations, we systematically investigated the crucial role of phase engineering and heteroatom incorporation in the dynamics of the catalytically active species and sites of CoSe$_2$ model catalysts (i.e. o-CoSe$_2$ with a marcasite-type structure, and c-CoSe$_2$ and c-S-CoSe$_2$ with pyrite-type structures) for overall water electrolysis in different media.

First, under acidic conditions, analysis of *operando* spectroscopic monitoring reveals that the electrochemical pre-activation process of o-CoSe$_2$ promotes surface corrosion with the removal of oxidized oxyanion species, and then the reconstructed o-CoSe$_2$ undergoes an electrochemically driven structural optimization into the generation of disordered catalytically active [CoSe$_6$] motifs for the H$_2$ release. In contrast, such surface corrosion along with electrochemically driven restructuring into active species was not observed in c-CoSe$_2$ and c-S-CoSe$_2$, which were demonstrated as stable catalysts throughout the entire acidic HER. Combinations of the aforementioned *operando* spectroscopic characterizations and DFT calculations elucidate that the acidic HER of o-CoSe$_2$ proceeds with the adsorption/desorption of H* intermediates at the Se sites within the defective [CoSe$_6$] motifs, which features a lower energy barrier compared to that of c-CoSe$_2$. Partial S incorporation in CoSe$_2$ not only enables a newly induced Co d-S p orbital hybridization with facilitated HER kinetics but also stabilizes the active S sites during the reaction process. As a result of the tuned HER kinetics, the as-prepared c-S-CoSe$_2$ catalysts demonstrated exceptional acidic HER performance with a low overpotential of -88 mV at -10 mA/cm^2 and robust electrochemical stability at 20 m/cm^2 for over 300 h.

To unravel the role of pH variations in the intrinsic HER kinetics, *operando* monitoring of three CoSe$_2$ catalysts (i.e. o-CoSe$_2$, c-CoSe$_2$, and c-S-CoSe$_2$) was also performed at pH 14. From our *operando* analysis, we observed a multi-step restructuring into metallic cobalt species in o-CoSe$_2$ toward the alkaline HER. Specifically, during the pre-activation process, the interaction reaction between o-CoSe$_2$ and the alkaline medium results in the formation of rich oxidized species covered on its surface; upon cathodic polarizations, these

oxidized species further convert into metallic Co species, which serve as the true active species for the alkaline HER. DFT simulations corroborate that these *in situ*-generated metallic Co species in alkaline media exhibit a high energy barrier for the H_2 release compared to acidic conditions. Consequently, o-$CoSe_2$ displays poor HER performance at pH 14 than at pH 0. Notably, combined above *operando* spectroscopic monitoring and DFT calculations demonstrate that c-$CoSe_2$ and c-S-$CoSe_2$ are thermodynamically more stable than o-$CoSe_2$. These catalysts retain their structural integrity well throughout the entire alkaline HER. On this basis, the as-prepared c-S-$CoSe_2$ catalysts excel through excellent alkaline HER performance with a low overpotential of -121 mV (-10 m/cm^2) and robust electrochemical durability for over 300 h with any obvious changes.

Concerning the OER, we show that all $CoSe_2$ catalysts undergo similar restructuring into high-valent CoO_2 species with rich structural disorders, serving as the real catalytically active species. On the other hand, our *operando* results also reveal that the surface oxidized oxyanion species experience complete leaching into the electrolyte prior to the OER, indicating that they do not play a role in the OER. This conclusion is further evident from electrochemical characterization with reference o-P-$CoSe_2$ catalysts. Caution needs to be exercised that precise unveiling of the dynamics of the local electronic structures of the oxidized anionic components (i.e. SO_x^- and SO_x^-) during the HER/OER processes still needs to be addressed in future related studies. In this context, we believe that *operando* spectroelectrochemical investigations focusing on the local coordination geometries of the anionic species are essential.

Conflict of interest

The authors declare no conflict of interest.

Reference

[1] J. N. Hausmann, R. Schlögl, P. W. Menezes, M. Driess, *Energy Environ. Sci.* **2021**, *14*, 3679.

[2] Y. Zhao, D. P. Adiyeri Saseendran, C. Huang, C. A. Triana, W. R. Marks, H. Chen, H. Zhao, G. R. Patzke, *Chem. Rev.* **2023**, *123*, 6257.

[3] K. Kawashima, A. E. F. Milton, J. S. Archer, D. T. Collins, N. L. Serrat, C. E. Chukwuneke, R. A. Marquez, L. A. Smith, C. B. Mullins, *ACS Energy Lett.* **2024**, *9*, 6126.

[4] a) F. Liu, C. Shi, X. Guo, Z. He, L. Pan, Z.-F. Huang, X. Zhang, J.-J. Zou, *Adv. Sci.* **2022**, *9*, 2200307; b) Z.-F. Huang, J. Wang, Y. Peng, C.-Y. Jung, A. Fisher, X. Wang, *Adv. Energy Mater.* **2017**, *7*, 1700544.

[5] K. Kawashima, R. A. Márquez, L. A. Smith, R. R. Vaidyula, O. A. Carrasco-Jaim, Z. Wang, Y. J. Son, C. L. Cao, C. B. Mullins, *Chem. Rev.* **2023**, *123*, 12795.

[6] W. Zheng, M. Liu, L. Y. S. Lee, *ACS Catal.* **2020**, *10*, 81.

[7] a) W. Wan, S. Wei, J. Li, C. A. Triana, Y. Zhou, G. R. Patzke, *J. Mater. Chem. A* **2019**, *7*, 15145; b) W. Du, Y. Shi, W. Zhou, Y. Yu, B. Zhang, *Angew. Chem. Int. Ed.* **2021**, *60*, 7051.

[8] Y. Zhao, W. Wan, R. Erni, L. Pan, G. R. Patzke, *Angew. Chem. Int. Ed.* **2024**, *63*, e202400048.

[9] a) Y. Sun, J. Wu, Z. Zhang, Q. Liao, S. Zhang, X. Wang, Y. Xie, K. Ma, Z. Kang, Y. Zhang, *Energy Environ. Sci.* **2022**, *15*, 633; b) Z.-F. Huang, J. Song, K. Li, M. Tahir, Y.-T. Wang, L. Pan, L. Wang, X. Zhang, J.-J. Zou, *J. Am. Chem. Soc.* **2016**, *138*, 1359; c) S. Zhuo, Y. Shi, L. Liu, R. Li, Le Shi, D. H. Anjum, Y. Han, P. Wang, *Nat. Commun.* **2018**, *9*, 3132.

[10] Y. Zhu, H.-C. Chen, C.-S. Hsu, T.-S. Lin, C.-J. Chang, S.-C. Chang, L.-D. Tsai, H. M. Chen, *ACS Energy Lett.* **2019**, *4*, 987.

[11] Y. Zhao, W. Wan, Y. Chen, R. Erni, C. A. Triana, J. Li, C. K. Mavrokefalos, Y. Zhou, G. R. Patzke, *Adv. Energy Mater.* **2020**, *10*, 2002228.

[12] S. Zhao, Y. Wang, J. Dong, C.-T. He, H. Yin, P. An, K. Zhao, X. Zhang, C. Gao, L. Zhang et al., *Nat. Energy* **2016**, *1*, 16184.

[13] Y. Zhao, W. Wan, N. Dongfang, C. A. Triana, L. Douls, C. Huang, R. Erni, M. Iannuzzi, G. R. Patzke, *ACS Nano* **2022**, *16*, 15318.

[14] a) P. W. Menezes, S. Yao, R. Beltrán-Suito, J. N. Hausmann, P. V. Menezes, M. Driess, *Angew. Chem. Int. Ed.* **2021**, *60*, 4640; b) J. N. Hausmann, R. A. Khalaniya, C. Das, I. Remy-Speckmann, S. Berendts, A. V. Shevelkov, M. Driess, P. W. Menezes, *Chem. Commun.* **2021**, *57*, 2184.

[15] T. Tian, H. Gao, X. Zhou, L. Zheng, J. Wu, K. Li, Y. Ding, *ACS Energy Lett.* **2018**, *3*, 2150.

[16] R. Zhang, L. Pan, B. Guo, Z.-F. Huang, Z. Chen, L. Wang, X. Zhang, Z. Guo, W. Xu, K. P. Loh et al., *J. Am. Chem. Soc.* **2023**, *145*, 2271.

[17] a) Z.-F. Huang, S. Xi, J. Song, S. Dou, X. Li, Y. Du, C. Diao, Z. J. Xu, X. Wang, *Nat. Commun.* **2021**, *12*, 3992; b) T. Zhang, J. Jiang, W. Sun, S. Gong, X. Liu, Y. Tian, D. Wang, *Proc. Natl. Acad. Sci. U.S.A.* **2024**, *121*, e2317247121.

[18] a) T. Tian, M. Zheng, J. Lin, X. Meng, Y. Ding, *Chem. Commun.* **2019**, *55*, 1044; b) Z.-F. Huang, J. Song, Y. Du, S. Xi, S. Dou, J. M. V. Nsanzimana, C. Wang, Z. J. Xu, X. Wang, *Nat. Energy* **2019**, *4*, 329; c) H. Jia, N. Yao, Z. Liao, L. Wu, J. Zhu, Y. Lao, W. Luo, *Angew. Chem. Int. Ed.* **2024**, *63*, e202408005; d) Y. Ou, L. P. Twight, B. Samanta, L. Liu, S. Biswas, J. L. Fehrs, N. A. Sagui, J. Villalobos, J. Morales-Santelices, D. Antipin et al., *Nat. Commun.* **2023**, *14*, 7688.

[19] S. Wang, Q. Jiang, S. Ju, C.-S. Hsu, H. M. Chen, Di Zhang, F. Song, *Nat. Commun.* **2022**, *13*, 6650.

[20] Y. Zhao, N. Dongfang, C. A. Triana, C. Huang, R. Erni, W. Wan, J. Li, D. Stoian, L. Pan, P. Zhang et al., *Energy Environ. Sci.* **2022**, *15*, 727.

[21] a) M. Hou, L. Zheng, Di Zhao, X. Tan, W. Feng, J. Fu, T. Wei, M. Cao, J. Zhang, C. Chen, *Nat. Commun.* **2024**, *15*, 1342; b) X. Jin, H. Jang, N. Jarulertwathana, M. G. Kim, S.-J. Hwang, *ACS Nano* **2022**, *16*, 16452.

[22] B. R. Wygant, K. Kawashima, C. B. Mullins, *ACS Energy Lett.* **2018**, *3*, 2956.

[23] J. N. Hausmann, P. W. Menezes, *Angew. Chem. Int. Ed.* **2022**, *61*, e202207279.

[24] J. Timoshenko, B. Roldan Cuenya, *Chem. Rev.* **2021**, *121*, 882.

[25] a) J. Song, Z.-X. Qian, J. Yang, X.-M. Lin, Q. Xu, J.-F. Li, *ACS Energy Lett.* **2024**, *9*, 4414; b) Y. Zhu, J. Wang, H. Chu, Y.-C. Chu, H. M. Chen, *ACS Energy Lett.* **2020**, *5*, 1281.

[26] X.-L. Zhang, P.-C. Yu, X.-Z. Su, S.-J. Hu, L. Shi, Y.-H. Wang, P.-P. Yang, F.-Y. Gao, Z.-Z. Wu, L.-P. Chi et al., *Sci. Adv.*, *9*, eadh2885.

[27] Y. Dou, C.-T. He, L. Zhang, H. Yin, M. Al-Mamun, J. Ma, H. Zhao, *Nat. Commun.* **2020**, *11*, 1664.

[28] X.-L. Zhang, S.-J. Hu, Y.-R. Zheng, R. Wu, F.-Y. Gao, P.-P. Yang, Z.-Z. Niu, C. Gu, X. Yu, X.-S. Zheng et al., *Nat. Commun.* **2019**, *10*, 5338.

[29] Y. Sun, X. Li, T. Zhang, K. Xu, Y. Yang, G. Chen, C. Li, Y. Xie, *Angew. Chem. Int. Ed.* **2021**, *60*, 21575.

[30] Y.-R. Zheng, P. Wu, M.-R. Gao, X.-L. Zhang, F.-Y. Gao, H.-X. Ju, R. Wu, Q. Gao, R. You, W.-X. Huang et al., *Nat. Commun.* **2018**, *9*, 2533.

[31] R. Sun, M. K. Y. Chan, G. Ceder, *Phys. Rev. B* **2011**, *83*, 235311.

[32] P. Chen, K. Xu, S. Tao, T. Zhou, Y. Tong, H. Ding, L. Zhang, W. Chu, C. Wu, Y. Xie, *Adv. Mater.* **2016**, *28*, 7527.

[33] S. G. Lyapin, A. N. Utyuzh, A. E. Petrova, A. P. Novikov, T. A. Lograsso, S. M. Stishov, *J. Phys.: Condens. Matter* **2014**, *26*, 396001.

[34] V. V. Poborchii, A. V. Kolobov, K. Tanaka, *Appl. Phys. Lett.* **1998**, *72*, 1167.

[35] W. Zheng, *ACS Energy Lett.* **2023**, *8*, 1952.

[36] Y. Shi, W. Du, W. Zhou, C. Wang, S. Lu, S. Lu, B. Zhang, *Angew. Chem. Int. Ed.* **2020**, *59*, 22470.

[37] C. E. Lund Myhre, D. H. Christensen, F. M. Nicolaisen, C. J. Nielsen, *J. Phys. Chem. A* **2003**, *107*, 1979.

[38] Y. Hu, C. Hu, A. Du, T. Xiao, L. Yu, C. Yang, W. Xie, *Anal. Chem.* **2023**, *95*, 1703.

[39] Z. Xiao, Y.-C. Huang, C.-L. Dong, C. Xie, Z. Liu, S. Du, W. Chen, D. Yan, L. Tao, Z. Shu et al., *J. Am. Chem. Soc.* **2020**, *142*, 12087.

[40] N. Yao, G. Wang, H. Jia, J. Yin, H. Cong, S. Chen, W. Luo, *Angew. Chem. Int. Ed.* **2022**, *61*, e202117178.

[41] a) M. Risch, F. Ringleb, M. Kohlhoff, P. Bogdanoff, P. Chernev, I. Zaharieva, H. Dau, *Energy Environ. Sci.* **2015**, *8*, 661; b) J. N. Hausmann, S. Mebs, K. Laun, I. Zebger, H. Dau, P. W. Menezes, M. Driess, *Energy Environ. Sci.* **2020**, *13*, 3607.

[42] a) A. Moysiadou, S. Lee, C.-S. Hsu, H. M. Chen, X. Hu, *J. Am. Chem. Soc.* **2020**, *142*, 11901; b) X. Zhao, Y. Li, Y. Cui, M. Saqib, X. Zhang, R. Hao, Z. Zheng, *J. Am. Chem. Soc.* **2023**, *145*, 20897; c) W. H. Lee, M. H. Han, Y.-J. Ko, B. K. Min, K. H. Chae, H.-S. Oh, *Nat. Commun.* **2022**, *13*, 605.

[43] P. Ye, K. Fang, H. Wang, Y. Wang, H. Huang, C. Mo, J. Ning, Y. Hu, *Nat. Commun.* **2024**, *15*, 1012.

[44] B. Dasgupta, S. Yao, I. Mondal, S. Mebs, J. Schmidt, K. Laun, I. Zebger, H. Dau, M. Driess, P. W. Menezes, *ACS Nano* **2024**, *18*, 33964.

[45] a) Y. Liu, T. Sakthivel, F. Hu, Y. Tian, D. Wu, E. H. Ang, H. Liu, S. Guo, S. Peng, Z. Dai, *Adv. Energy Mater.* **2023**, *13*, 2203797; b) J. Wang, X. Li, B. Wei, R. Sun, W. Yu, H. Y. Hoh, H. Xu, J. Li, X. Ge, Z. Chen et al., *Adv. Funct. Mater.* **2020**, *30*, 1908708.